

Cite this article as: Wang Zhengjun, Dong Chen, Wang Ziyang, et al. Thermal Fatigue Crack Initiation and Propagation Behavior of Multicomponent Al-7Si-0.3Mg Alloys[J]. Rare Metal Materials and Engineering, 2022, 51(03): 783-792.

ARTICLE

# Thermal Fatigue Crack Initiation and Propagation Behavior of Multicomponent Al-7Si-0.3Mg Alloys

Wang Zhengjun<sup>1,2</sup>, Dong Chen<sup>1,2</sup>, Wang Ziyang<sup>1</sup>, Zhang Qiuyang<sup>1,2</sup>, Liu Jingjing<sup>1,2</sup>, Chen Xiaogang<sup>1,2</sup>

<sup>1</sup> Huaiyin Institute of Technology, Huai'an 223003, China; <sup>2</sup> Jiangsu Key Laboratory of Advanced Manufacturing Technology, Huai'an 223003, China

**Abstract:** The thermal fatigue properties of multicomponent Al-7Si-0.3Mg aluminum alloys in three different treatment states at different temperatures were studied. The integral method and secant method were proposed to calculate the thermal fatigue crack propagation life, and the thermal fatigue crack growth behavior of the alloys was analyzed. The results indicate that the temperature change has a direct effect on the thermal fatigue crack propagation rate of the multicomponent Al-7Si-0.3Mg aluminum alloys. The thermal fatigue properties of the multicomponent Al-7Si-0.3Mg alloys with addition of Cu, Mn, Ti, and other elements after refinement and direct refinement are superior to those of the as-cast Al-7Si-0.3Mg alloys. The growth behavior of thermal fatigue cracks mainly includes the initiation and propagation of thermal cracks. The initiation of thermal fatigue crack requires a certain incubation period and the crack is generated at the V-notch. When the alternating thermal stress exceeds the yield strength  $\sigma_s$  of alloys, different types of thermal fatigue cracks appear at the stress concentration parts or at defects of the V-notch but with only one main crack. When the angle between the crack tip propagation path and the major axis direction of the second phase particle is less than  $45^\circ$ , the crack propagation extends further along the edge of the second phase particles; when the angle between the crack tip propagation path and the minor axis direction of the second phase particle is less than  $45^\circ$ , the crack passes through the second phase particle and extends forward.

**Key words:** multicomponent Al-7Si-0.3Mg aluminum alloy; thermal fatigue; initiation; crack propagation life calculation; propagation path

The automotive engines with higher power output and less fuel consumption are commonly required as a primary consideration for engine design<sup>[1-4]</sup>. Thus, the development of lightweight materials attracts much attention. The high-quality aluminum and its alloys have exceptional performance and are widely used in current automotive industry<sup>[5-8]</sup>. The hypoeutectic Al-Si-Mg alloys are widely used in aviation and aerospace, especially in automotive fields, because of their high specific strength, good castability, and thermal fatigue resistance<sup>[9-12]</sup>. At present, Al-Si-Mg alloy is usually used as the cylinder blocks and cylinder heads for the core components of automobile engine. The gap between these two

components is small after heating due to their similar thermal expansion coefficients, therefore reducing the thermal stress and noise caused by the cold and hot shocks. However, the thick plate-like eutectic silicon in as-cast hypoeutectic Al-Si-Mg alloys may crack severely and destroy the continuity of the matrix, which easily produces the stress concentration at the tip and corner of eutectic silicon, resulting in a significant degradation of the mechanical properties, especially the elongation<sup>[13,14]</sup>. To achieve better mechanical properties of the cylinder block of aluminum alloys, the composite refinement and modification methods are adopted for as-cast aluminum alloys with high strength and toughness<sup>[15-18]</sup>. Researches

Received date: March 21, 2021

Foundation item: National Natural Science Foundation of China (51701079); Doctoral Scientific Research Start-up Foundation from Huaiyin Institute of Technology (Z301B18558); Enterprise-University-Research Institute Collaboration Project of Jiangsu Province (BY2019153); Natural Science Foundation of Jiangsu Province (BK20201066); Natural Science Research Project of Jiangsu Provincial Higher Education Institutions (20KJB410004); Natural Science Research of Institution of Higher Education of Jiangsu Province (17KJA460003)

Corresponding author: Wang Zhengjun, Ph. D., Associate Professor, Faculty of Mechanical and Material Engineering, Huaiyin Institute of Technology, Huai'an 223003, P. R. China, Tel: 0086-517-83559196, E-mail: wangzjhyit@hyit.edu.cn

Copyright © 2022, Northwest Institute for Nonferrous Metal Research. Published by Science Press. All rights reserved.

indicate that the excellent refinement and modification effects can be combined in the hypoeutectic Al-Si-Mg alloy through the combination of rare earth (RE)-containing Al-5Ti-1B master alloys and Al-10Sr master alloys, which can significantly improve the microstructure and mechanical properties<sup>[19-23]</sup>. As the engine is subjected to high thermal strain during the launch, flameout, acceleration, or deceleration, the power coefficient of the engine is increased. Therefore, there are stringent requirements for the thermal fatigue properties of engine materials<sup>[24]</sup>. However, the commonality and regularity of aluminum alloys in terms of the thermal fatigue performance are rarely investigated<sup>[25]</sup>. The prediction of the thermal fatigue life of multicomponent aluminum alloys lacks an effective method<sup>[26]</sup>. In this research, the multicomponent hypoeutectic Al-7Si-0.3Mg alloys for cylinder block fabrication were studied. The thermal fatigue tests were conducted on the LRP1200 fatigue tester, and the thermal fatigue properties of Al-7Si-0.3Mg alloys under different temperatures were studied. A method to calculate the thermal fatigue life was proposed, and the relationship among the thermal fatigue crack initiation, propagation path, and propagation rate was analyzed, providing a theoretical basis to improve the thermal fatigue properties of the as-cast Al-7Si-0.3Mg alloys. This research also offers an important reference value for the study of thermal fatigue properties of other materials.

## 1 Experiment

The Al-7Si-0.3Mg alloys with Cu and Ti addition after three different treatments of casting, direct refinement, and refinement were tested and regarded as specimen A, specimen B, and specimen C, respectively. The composition of the as-cast alloys is as shown in Table 1. At 750 °C, the KSL-12-JY resistance furnaces were used to melt and prepare the alloys. The melt of specimen A was degassed and refined at 730 °C, and then cast. The specimen B and C were also refined at 730 °C and modified by adding 0.80wt% Al-5Ti-1B-1RE (RE: La and Ce) and 0.30wt% Al-10Sr master alloy melts, respectively. The melt was poured into the wedge-shaped metal molds at 730 °C, and the thermal fatigue specimens were wire cut, as shown in Fig.1. The thermal fatigue test was conducted using an LRP1200 fatigue tester. Three specimens were examined at different temperatures to analyze the features of the fatigue cracks.

Meanwhile, the standard tensile specimens were prepared by wire-electrode cutting according to GB/T 228.1-2010. The tensile mechanical properties were tested on the electronic universal testing machine (CSS-44100), and the tensile rate was 1.00 mm/min. The Vickers microhardness test of the

specimens was conducted on the HV-1000 microhardness tester under the conditions of the square conical diamond head with a relative surface angle of 136° partially pressed into the specimen surface, the pressure of 2450 N, and holding time of 30 s. The impact toughness test of the specimens was conducted on a JBGD-300 high/low-temperature impact tester with the impact velocity of 5.2 m/s, pendulum pre-elevation angle of 150°, pendulum axis-to-impact point distance of 750 mm, impact cutter angle of 30°, and support span of 40 mm. The size of the impact test specimens was 10±0.1 mm in thickness and width, and 55±0.6 mm in length. U-type grooves with a width and depth of 2±0.05 mm were produced in the middle of every specimen surface.

For uniform heating of the specimen in the thermal fatigue test, the temperature was held for 5 min after reaching the designed temperature. The lower limit of temperature was determined as 20 °C by the metal sheet thermal fatigue test method<sup>[27]</sup> (the temperature of the cooling water). Thus, the lower limit of temperature in test was 20 °C (circulating cooling water temperature), and the thermal fatigue test was conducted at the temperature range with different upper limit temperatures: 20~300, 20~350, and 20~400 °C. The effects of different temperature ranges on the thermal fatigue properties of Al-7Si-0.3Mg alloys were studied. The schematic diagram of the thermal cycle process is shown in Fig.2. A complete heating-cooling cycle can be represented by  $O_i \rightarrow A_i \rightarrow B_i \rightarrow C_i$  ( $i = 1, 2, 3, \dots$ ). Although the upper limit temperatures were different, leading to different temperature raising rates, the shapes of the temperature curves were similar. The lower limit temperature of the test was  $T_{\min} = 20$  °C and the upper limit temperature was  $T_{\max} = 300, 350, 400$  °C. The holding duration  $t_1$  was 110 s, the cooling duration  $t_2$  was 10 s, and the total cycle duration was  $t = t_1 + t_2 = 120$  s.

The thermal fatigue specimens were removed and ground after a certain number of cycles and observed under a LEICADM 2500M optical microscope (OM). When the cracks appeared at the V-notch of specimens (the length of initial crack was 0.10 mm<sup>[28]</sup>), the crack length  $a$  was measured and the number of cycles  $N$  was recorded. When the crack length was more than 0.10 mm, the thermal fatigue cracks were propagated, and then the crack propagation path and characteristic location were observed and analyzed. The thermal fatigue crack propagation life could be obtained directly from the  $a-N$  curve.

## 2 Results and Discussion

### 2.1 Thermal fatigue crack growth

The thermal fatigue crack initiation period presented by the number of thermal fatigue cycles  $N$  of three different alloys at

Table 1 Chemical composition of original Al-7Si-0.3Mg alloys (wt%)

Specimen	Si	Mg	Cu	Mn	Fe	Ti	B	RE	Sr	Various trace elements	Al
A	7.03	0.32	-	-	-	-	-	-	-	≤0.20	Bal.
B	7.03	0.32	-	-	-	0.042	0.0074	0.0086	0.032	≤0.20	Bal.
C	6.92	0.29	1.85	0.33	0.08	0.29	0.0076	0.0082	0.034	≤0.20	Bal.

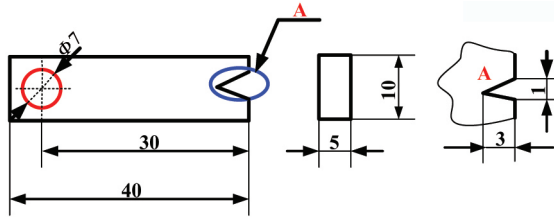


Fig.1 Schematic diagrams of thermal fatigue specimens

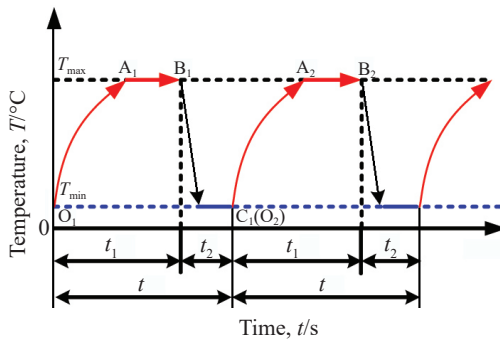


Fig.2 Schematic diagram of thermal cycles

different temperature ranges is shown in Table 2. The temperature range has an important influence on the thermal fatigue crack initiation period of multicomponent Al-7Si-0.3Mg alloys. In the same temperature range, the crack initiation period of as-cast specimen A, specimen B, and specimen C is the shortest, medium, and the longest, respectively. The crack initiation period of each thermal fatigue specimen is the longest, medium, and the shortest at the temperature range of 20~300, 20~350, and 20~400 °C, respectively.

Fig. 3 shows that the crack growth basically presents the S-shaped curve under different temperature ranges. As the upper limit of temperature decreases, the S-shape of curves becomes more obvious. The lower the upper limit temperature, the longer the crack initiation period (crack length  $a < 0.10$  mm); the higher the upper limit temperature, the shorter the crack initiation period (crack length  $a < 0.10$  mm). The crack propagation period is shorter than the crack

Table 2 Thermal fatigue crack initiation period  $N$  of specimens in different temperature ranges

Temperature range/°C	Specimen A	Specimen B	Specimen C
20~300	19 800	22 000	23 800
20~350	8300	9200	10 600
20~400	3000	4200	5700

initiation period which is the main stage in thermal fatigue crack propagation process and the determining factor of thermal fatigue crack propagation life. In the final stage of thermal fatigue crack propagation, the crack propagation rate  $da/dN$  is gradually decreased with increasing the crack length, and finally the propagation stops. The  $da/dN=0$  can be achieved with less thermal fatigue cycles, and therefore the crack propagation period is not long. It can be seen from Fig.3a that when the temperature range is 20~300 °C and the number of thermal fatigue cycles is 20 000, specimen A has an obvious crack with the crack length of 0.11 mm, specimen B has a relatively short crack with crack length of 0.02 mm, while specimen C does not produce any crack. However, with the thermal fatigue cycles further proceeding, the crack length of all specimens is increased significantly. When the number of thermal fatigue cycles is 27 500, the crack length of specimen A increases rapidly to 1.03 mm, and that of specimen B is 0.61 mm. Meanwhile, the crack propagation period of specimen C is relatively short and its crack length is only 0.30 mm, which indicates that the thermal fatigue resistance of specimen C is significantly better than that of specimen A and B at 300 °C. The growth rate of cracks is increased firstly and then decreased with increasing the number of thermal fatigue cycles<sup>[29-31]</sup> because of the approximate exponential relationship between  $a$  and  $N$  in the crack propagation zone after the crack initiation period. The crack propagation rate  $da/dN$  is controlled by the intensity range of crack tip thermal stress  $\Delta K = Y \sqrt{a} \sigma$  and satisfies the Paris formula<sup>[32]</sup> of power function relationship, as follows:

$$\frac{da}{dN} = c(\Delta K)^n = c(K_{max} - K_{min})^n = c(Y \sqrt{a} \sigma_{max} - Y \sqrt{a} \sigma_{min})^n = c(Y \sqrt{a} \sigma)^n \quad (1)$$

where  $\Delta K$  is the intensity range of crack tip stress (field);  $Y$  is

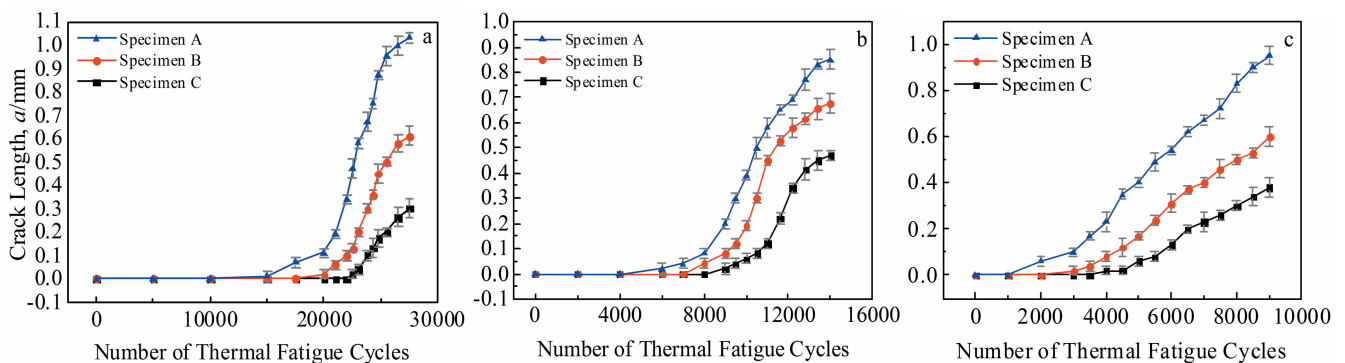


Fig.3 Thermal fatigue lives of different specimens in different temperature ranges: (a) 20~300 °C, (b) 20~350 °C, and (c) 20~400 °C

the crack shape factor of 1~2;  $\sigma_{\max}$  and  $\sigma_{\min}$  represent the maximum stress and minimum stress, respectively;  $a$  is the crack length;  $c$  and  $n$  ( $n=2\sim4$  for most materials) are constants determined by the intercept and slope of the  $\lg(da/dN)$ - $\lg\Delta K$  curve, respectively.

During the crack propagation, on the one hand, as the crack length  $a$  increases, the crack propagation rate is increased; on the other hand, as the local restraint ratio decreases, the thermal stress is relaxed and the crack propagation rate is decreased. Within a certain range, these two effects are offset by each other and thereby  $da/dN$  appears to be constant. The thermal fatigue crack propagation life can be calculated by the integral of Eq.(1), as follows:

$$dN = \frac{da}{c(Y\Delta\sigma)^n a^{\frac{n}{2}}} \quad (2)$$

$$N_c = \frac{da}{c(Y\Delta\sigma)^2 a^2} [\ln a_c - \ln a_0] \quad n=2 \quad (3)$$

$$N_c = \int_0^{N_c} dN = \int_{a_0}^{a_c} \frac{da}{c(Y\Delta\sigma)^n a^{\frac{n}{2}}} = \frac{2}{(n-2)c(Y\Delta\sigma)^n} \times \left[ \frac{1}{a_0^{\frac{n-2}{2}}} - \frac{1}{a_c^{\frac{n-2}{2}}} \right] \quad n \neq 2 \quad (4)$$

where  $a_0$  is the initial crack size,  $a_c$  is the critical crack size,  $N_c$  is number of cycles required from  $a_0$  to  $a_c$ , namely the thermal fatigue residual life.

According to the  $a$ - $N$  curves in Fig.3, the secant method can also be used to calculate the crack length or the number of thermal fatigue cycles required for a certain degree of crack propagation.

Based on the same  $a$ - $N$  curve, if  $a_i < a_k < a_{i+1}$ , then  $N_i < N_k < N_{i+1}$ , and the slope of two infinitely close data points on  $a$ - $N$  curve in the propagation stage can be calculated, and the crack propagation rate  $\frac{da}{dN} \approx \frac{\Delta a}{\Delta N} = \frac{a_{i+1} - a_i}{N_{i+1} - N_i}$ . Thus, Eq. (5) and

Eq.(6) can be obtained, as follows:

$$a_k = \frac{da}{dN} (N_k - N_i) \quad (5)$$

$$N_k = \frac{dN}{da} (a_k - a_i) \quad (6)$$

where  $a_i$  and  $a_k$  represent the crack length at  $i$  and  $k$  data points, respectively;  $N_i$  and  $N_k$  represent the number of thermal fatigue cycles at  $i$  and  $k$  data points, respectively.

According to Eq.(5), the crack length of specimens after a certain number of thermal fatigue cycles can be calculated. The number of thermal fatigue cycles required for a certain degree of crack propagation can also be calculated by Eq.(6), i.e., the thermal fatigue crack propagation life can be calculated.

Fig. 4 shows the number of thermal fatigue cycles required for crack initiation until  $a=0.10$  mm at the V-notch of three specimens in different temperature ranges. The slope of the fitting line in 300~350 °C region is significantly smaller than that in 350~400 °C region. The thermal fatigue resistance and the thermal fatigue life of the Al-7Si-0.3Mg alloys are both reduced, indicating that the thermal fatigue crack growth of alloys is greatly accelerated and the thermal fatigue life is decreased with increasing the upper limit temperature. Thus,

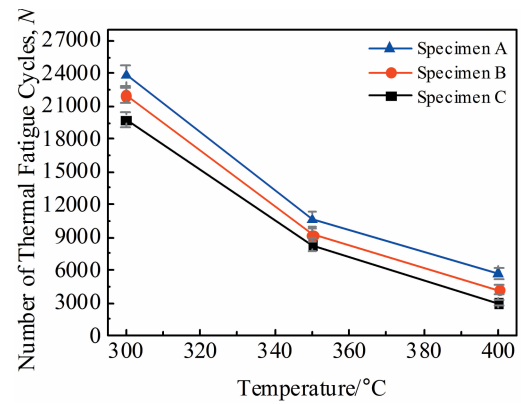


Fig.4 Number of thermal fatigue cycles required for crack initiation until crack length  $a=0.1$  mm of specimens in different temperature ranges

specimen C performs better thermal fatigue resistance than specimen A and specimen B do with the upper limit temperature of 300~400 °C. In general, the composition has a significant effect on the thermal fatigue life of Al-7Si-0.3Mg alloys in different temperature ranges.

## 2.2 Microstructures and mechanical properties

Fig. 5a shows the irregular  $\alpha$ -Al phase in as-cast specimen A. The morphology of eutectic silicon is thick plate-like or long needle-like. The length of eutectic silicon is 40~60  $\mu\text{m}$ , the width is 4~6  $\mu\text{m}$ , and the aspect ratio is more than 10. There is no obvious interface between the eutectic structure and primary  $\alpha$ -Al phase, and the distribution of the eutectic structure in the aluminum matrix is non-directional, irregular, and relatively scattered with the sharp edges.

The shape of the  $\alpha$ -Al phase in specimen B becomes more uniform and rounder, the size of  $\alpha$ -Al phase is finer, and the grain boundaries are clearer. The eutectic silicon phase is almost entirely transformed into the dispersed and fine fibrous structures and the lamellae almost disappear. The size of silicon phase decreases to 1~2  $\mu\text{m}$ , the contour becomes clear, and the distribution is mainly concentrated at the grain boundary, resulting in grain boundary strengthening effect, as shown in Fig.5b.

There are more secondary phases in specimen C, as shown in Fig.5c. The  $\alpha$ -Al phases of A area in specimen C become uniform, fine, and round, as indicated by Fig. 5c and corresponding EDS analysis of area A in Fig.6a. The grain boundaries are clear and the eutectic silicon phases are fine and fibrous, as indicated by area B in Fig. 5c and corresponding EDS analysis in Fig. 6b. The second phase  $\text{Al}_2\text{Cu}$  with smaller size and more uniform distribution is formed after adding Cu element, as indicated by area C in Fig. 5c and related EDS analysis in Fig. 6c. In the  $\text{Al}_2\text{Cu}$  and AlTi intermetallic compounds, the main components are the block-shaped AlSiTiCu phases with dispersed distribution, as indicated by area D in Fig. 5d and related EDS analysis in Fig. 6d. The Mn-containing phases, such as AlSiMnCuFe with round rod or strip shape, appear at both ends and are smaller

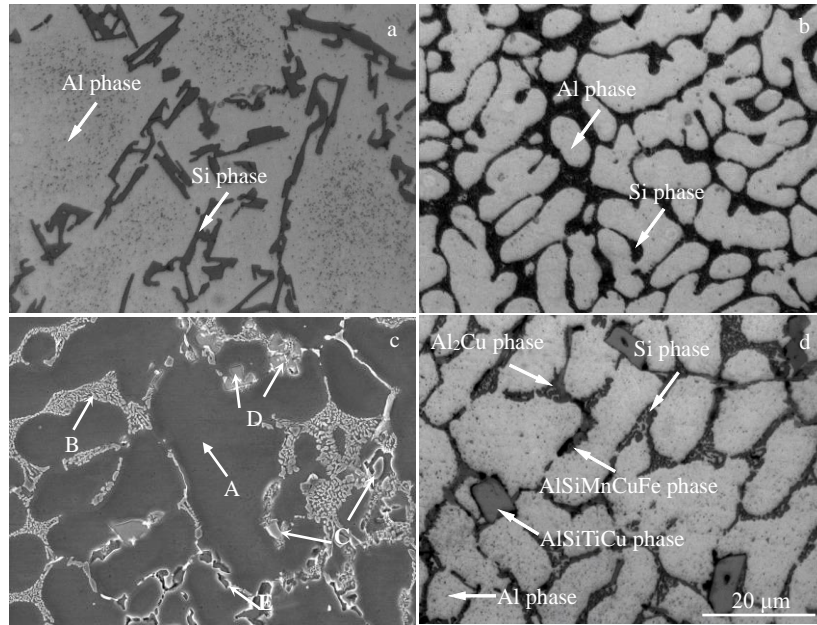


Fig.5 OM microstructures of specimen A (a), specimen B (b), specimen C (d) and SEM microstructure of specimen C (c)

than the AlSiTiCu phases, as indicated by area E and corresponding EDS analysis in Fig. 6e. The morphologies of different phases are clearly observed in Fig.5d.

The microstructures of aluminum alloys treated by different processes are obviously different. The mechanical properties of different specimens are shown in Fig.7. It can be seen that the mechanical properties of specimen B and specimen C after refinement and modification are obviously optimized than

those of specimen A. The splitting effect of the lamellar eutectic silicon on the alloy matrix is greatly reduced, and the stress concentration at the tip and corner of the eutectic silicon is also significantly reduced. The mechanical properties of Al-7Si-0.3Mg alloys, especially the elongation and impact toughness, are significantly improved after refinement and modification. The elongation  $\delta$  of different specimens is sorted from the largest to the smallest as 7.73%, 6.96%, and

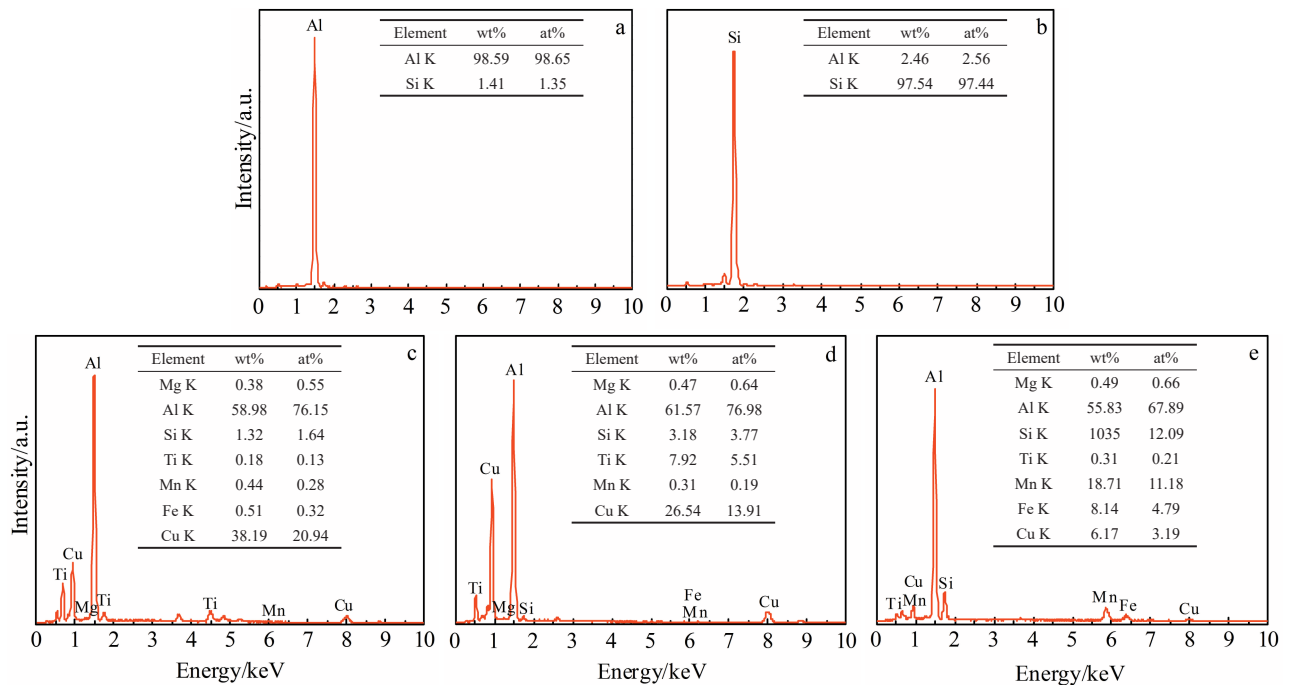


Fig.6 EDS analyses of different areas in specimen C in Fig.5c: (a) area A, (b) area B, (c) area C, (d) area D, and (e) area E

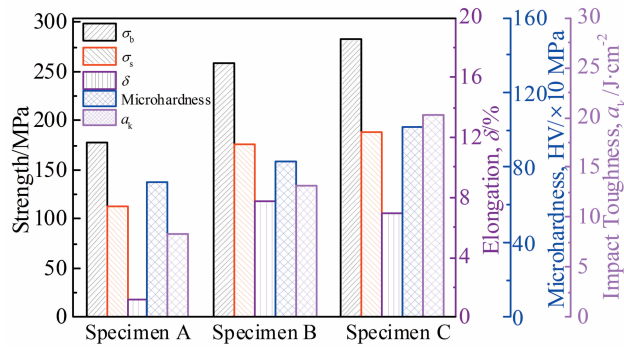


Fig.7 Mechanical properties of different specimens

1.17% for specimen B, specimen C, and specimen A, respectively. The tensile strength  $\sigma_b$ , yield strength  $\sigma_s$ , microhardness HV, and impact toughness  $a_k$  of specimen C are 282.36 MPa, 185.89 MPa, 1018 MPa, and 20.31 J·cm<sup>-2</sup>, respectively. These mechanical properties are increased by 59.02%, 68.32%, 40.41%, and 142.94% compared with those of specimen A, and by 9.13%, 7.10%, 22.05%, and 53.98% compared with those of specimen B, respectively.

There are more secondary phase particles in the refined and modified specimen C, which greatly change the component structure and become the strengthening phases, thereby effectively hindering the dislocation motion and greatly improving the mechanical properties of alloys. Different microstructures and mechanical properties of the three multicomponent Al-7Si-0.3Mg alloys lead to different thermal fatigue crack initiation and propagation behavior. The Al-7Si-0.3Mg alloys are effectively improved in the shape, size, quantity, and distribution of the secondary phase through refinement and modification, thereby improving their thermal fatigue resistance. At the occasion that the specified crack length is achieved, specimen B undergoes more thermal fatigue cycles than specimen A does. Because specimen C has more secondary phases, its grain boundaries are obviously refined and granulated, as shown in Fig.5c and 5d. Therefore, at the occasion that the specified crack length is achieved, specimen C undergoes much more thermal fatigue cycles than specimen A and specimen B do.

### 2.3 Incubation period of thermal fatigue crack

Since the normal working temperature of the cylinder block

is 20~300 °C and the thermal fatigue life curve of alloys in this temperature range has better accordance with the Paris formula, the temperature range of 20~300 °C is selected to study the initiation and propagation behavior of the thermal fatigue cracks in different alloys. The V-notch in each specimen is relatively flat before thermal fatigue cycling. It can be seen from Fig.8 that the grain size, eutectic silicon morphology, secondary dendrite arm spacing, secondary phase morphology, and secondary phase distribution in specimen B and specimen C are obviously superior to those in as-cast specimen A.

The crack initiation needs a certain incubation period, i.e., the crack appears after a certain number of thermal fatigue cycles. During the incubation period, the alloys undergo different degrees of plastic deformation, resulting in the depth variation, uneven surfaces, and even the occurrence of pits of different sizes and oxide layers on the edges of V-notches, as shown in Fig.9. Thus, the crack length of alloys after a certain number of thermal fatigue cycles can be specified and used as a standard to evaluate the thermal fatigue resistance of alloys treated by different processes. With increasing the number of thermal fatigue cycles, the size and number of pits are increased. Under the same conditions of temperature range and the number of thermal fatigue cycles of  $N=7000$ , the as-cast specimen A has numerous large and irregular pits on the edge of V-notch. The eutectic silicon phase is needle-like, as shown in Fig.9a. The V-notch of specimen B after direct refinement and modification has an obvious oxide layer with less pits of smaller sizes at different positions, compared with those of as-cast specimen A, as shown in Fig.9b. The eutectic silicon structure is refined and modified more obviously compared with that of as-cast specimen A. Therefore, the thermal fatigue resistance of specimen B is improved obviously. The pits in the V-notch of specimen C are smaller in size and less in number, compared with those in specimen B and specimen C, as shown in Fig.9c. The main reason is that the further addition of Cu, Mn, and Ti into specimen C can improve the strength, toughness, hardness, and high-temperature properties of the Al-7Si-0.3Mg alloys. The addition amount of copper and magnesium is sufficient and beneficial for generation of more Al<sub>2</sub>Cu and AlSiTiCu phases, thereby improving the heat resistance of specimen C. The

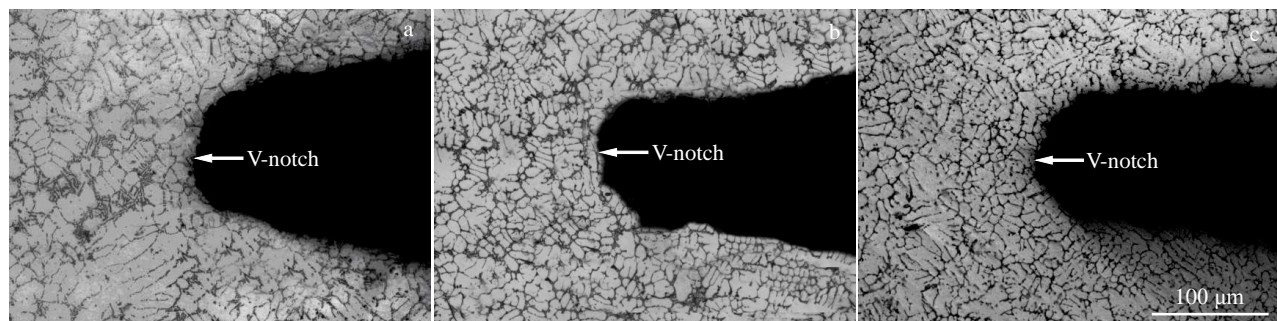


Fig.8 Microstructures of specimen A (a), specimen B (b), and specimen C (c) before thermal fatigue cycling ( $N=0$ )

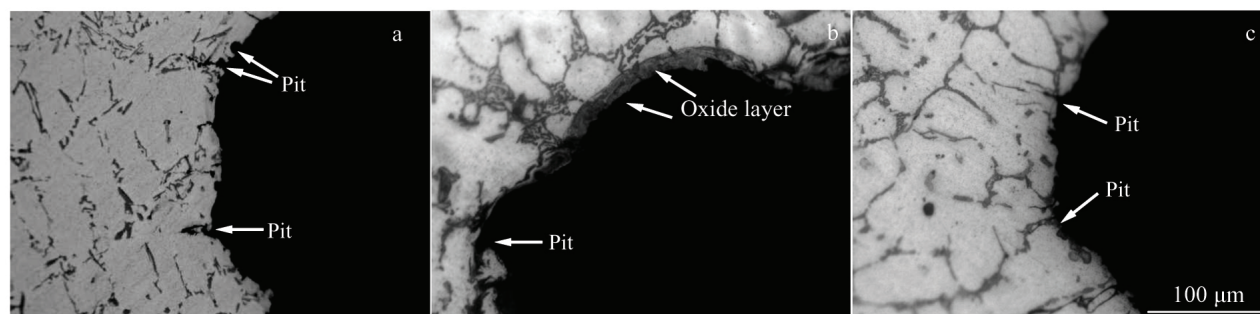


Fig.9 Microstructures of specimen A (a), specimen B (b), and specimen C (c) after thermal fatigue cycles of  $N=7000$

element Mn possesses the supersaturated solid solution property during the crystallization. Meanwhile, a dispersed AlSiMnCuFe phase is formed, which enhances the strength at room temperature and heat resistance. The amount of Ti addition is usually 0.15wt%~0.35wt%. Excess or less Ti may lead to poor refinement effect and low toughness. Thus, the optimum addition amount of Ti is 0.25wt%, which can improve the as-cast structure, refine the  $\alpha$ -Al phase, and fully dissolve the Al<sub>2</sub>Cu and Mn-rich phases in the non-equilibrium ternary eutectic into  $\alpha$ -Al phase. These effects influence the grain boundary slip, improve the strength and hardness, and enhance the plasticity and fracture toughness of alloys.

It can also be seen from Fig.9 that the oxide layer and pits appear alternately. The oxide layer and pit offset each other in a cyclic relationship, i. e., the oxidation promotes the formation of pits, and in turn the pits accelerate the oxidation. Under the same thermal fatigue cycle conditions, the oxidation degree of alloys can also reflect the thermal deformation resistance of alloys. Thus, the thermal deformation resistance of specimen A is weak, resulting in the formation of numerous deep pits, while that of specimen C is strong, resulting in less shallow pits. The thermal deformation resistance of specimen B is intermediate and shows the presence of both oxide layers and pits. Therefore, under the same conditions, the oxidation degree, the number of pits, and the V-notch size of specimen C are significantly smaller than those of specimen A and specimen B, indicating that the specimens after different treatments produce different degrees

of oxide layer and pits, and their crack incubation periods are also different.

#### 2.4 Thermal fatigue crack initiation analysis

The size and number of thermal fatigue cracks are increased with increasing the number of thermal fatigue cycles, as shown in Fig.10. When the number of thermal fatigue cycles is 24 500, the length of thermal fatigue crack of different specimens is sorted from the largest to the smallest as specimen A>specimen B>specimen C. So it can be concluded that the plastic deformation resistance of different specimens is specimen C>specimen B>specimen A. Under the same conditions, there is no substantial difference in the initiation process of thermal cracks for the specimens treated by three different processes, i. e., at the V-notch, the thermal fatigue damage accumulates continuously with increasing the number of thermal fatigue cycles, and the stress concentration occurs in some local weak areas. When the alternating thermal stress exceeds the yield strength  $\sigma_s$  of the alloys, different types of thermal fatigue cracks occur at the stress concentration region or at defects of the V-notch. The yield strength  $\sigma_s$  and plastic deformation are extremely sensitive to the composition and microstructure of the alloys, which can be greatly improved by the grain refinement and the composition modification. The grain refinement can effectively hinder the dislocation movement by reducing the grain size and the length of dislocation cluster in the crystal grain, thereby improving the yield strength  $\sigma_s$ . The relationship between the yield strength  $\sigma_s$  and the grain diameter  $d$  is in accordance with the Hall-



Fig.10 Microstructures near the gap region of specimen A (a), specimen B (b), and specimen C (c) after thermal fatigue cycles of  $N=24\ 500$

Petch formula<sup>[31]</sup>, as follows:

$$\sigma_s = \sigma_i + k_y d^{-\frac{1}{2}} \quad (7)$$

where  $\sigma_i$  is the total resistance of dislocation in matrix determined by the crystal structure and dislocation density;  $k_y$  is the pinning constant to measure the contribution of grain boundary to strengthening, or the stress concentration factor at the end of the slip band where  $\sigma_i$  and  $k_y$  are material constants under a certain condition of temperature and strain rate;  $d$  is the average grain diameter.

It can be seen from Eq.(7) that the smaller the average grain diameter  $d$ , the larger the yield strength  $\sigma_s$  of alloys. The grain refinement can improve not only the strength of alloys, but also the plasticity and toughness, because under the same external force, the strain difference between the grain interior and the grain boundary of the fine grain is small and the deformation is relatively uniform. Crack barely forms due to the stress concentration, and so the alloys can withstand larger deformation before fracture and achieve larger elongation after fracture and section shrinkage. Since few cracks in the fine-grain metals are generated and propagated, more energies are absorbed in the fracture process, i. e., the fracture toughness of alloys is enhanced. Besides, the alloy exhibits high thermal fatigue properties due to the grain refinement. The width and length of the thermal fatigue cracks in specimen A is significantly larger than those in specimen B and specimen C, as shown in Fig. 10. Therefore, the plastic deformation resistance of specimen B and specimen C is obviously better than that of specimen A.

### 2.5 Thermal fatigue crack propagation path analysis

Due to the stress concentration at the tip of V-notch in different specimens, the thermal fatigue cracks are preferentially initiated at the bottom of the V-notch where the thermal strain accumulates. With the thermal fatigue cycles further proceeding, multiple initiation cracks are formed and propagated, but only one main crack appears as the thermal stress is large and the stress concentration is considerable. A few cracks are slowly formed in other parts due to the low stress concentration. As shown in Fig. 11, three pits expand into cracks ①, ②, and ③, but only the thermal crack ② at the V-notch bottom becomes the single main crack. Meanwhile, as the main crack is further propagated, a new microcrack ④

is formed. During the thermal fatigue cycling, the thermal fatigue sub-cracks appear along the uneven edge of the V-notch, which indicates that under the same average stress, the cracks are propagated along the direction with inferior mechanical properties.

The macroscopic cracks are formed through the formation, growth, and connection of microcracks which are caused by the uneven local slip. The main formation mechanism of thermal fatigue microcracks is the surface slip zone cracking, grain boundary or sub-grain boundary cracking, and inclusions or interface cracking. The presence of silicon phase (the secondary phase) hinders the dislocation slip, thereby causing the uneven plastic deformation of the matrix. This phenomenon is mainly due to the local plastic constraints of the secondary phases, which result in strengthening and hindrance of the recovery from elasticity of the surrounding matrix, therefore leading to the residual compressive stress. Then the residual compressive stress is superimposed on the thermal fatigue crack, leading to the early closure of the crack and the decrease in  $\Delta K$ . According to Eq.(1), it can be seen that with decreasing the  $\Delta K$ ,  $da/dN$  is decreased, which agrees well with the above analysis result. From the thermal fatigue cycle tests, when the silicon phase, AlSiTiCu, or Al<sub>2</sub>Cu phase is distributed on the Al alloy matrix, the closure effect of the thermal fatigue crack can be increased, and the thermal fatigue crack propagation life is significantly improved. The crack propagation is a slow process with continuous energy consumption. The crack propagation plane is parallel to the maximum shear stress direction and at an angle of 45° to the principal stress direction. The orientation of the secondary phase particle also shows an important effect on the crack propagation path. If the crack tip propagation path is at an angle of less than 45° to the major axis direction of the secondary phase particle, as indicated by crack ① in Fig. 12, greater driving forces are required for the cracks to penetrate the secondary phase particles. When the driving force for crack propagation is insufficient to pass through the secondary phase particles, according to the principle of minimum energy dissipation of crack propagation, the crack expands preferentially and continues to move forward along the upper edge of the secondary phase particle. If the crack tip propagation path is at an angle of less than 45° from the minor

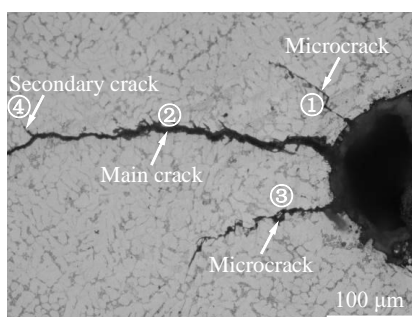


Fig.11 Propagation path of microcracks

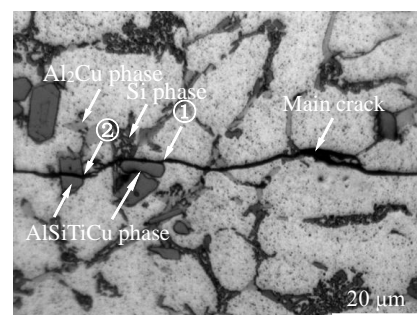


Fig.12 Thermal fatigue crack propagation path on Al alloy matrix

axis direction of the secondary phase particle, as indicated by crack ② in Fig. 12, the crack tip propagation has sufficient driving force, and the crack passes through the secondary phase particles and continues to propagate forward. When the crack tip extends beyond the large plastic zone, the thermal fatigue crack is propagated normally and continues to expand as the stress is released without concentration.

### 3 Conclusions

1) The plastic deformation resistance and the crack initiation duration of the Al-7Si-0.3Mg alloys after direct refinement and refinement are significantly improved compared with those of the as-cast Al-7Si-0.3Mg alloys. The thermal fatigue crack initiation duration is the longest, medium, and the shortest in the thermal fatigue temperature range of 20~300, 20~350, and 20~400 °C, respectively.

2) The integral method and secant method can be used to calculate the thermal fatigue life of machine parts with cracks or defects.

3) Due to the stress concentration at the V-notch tip of the thermal fatigue specimens, the thermal fatigue cracks are preferentially initiated at the V-notch bottom with the accumulation of thermal strain. With the thermal fatigue cycling further proceeding, multiple initiation cracks are formed, but only one main crack appears.

4) When the crack tip forms an angle of less than 45° with the major or minor axis direction of the secondary phase particles, the crack continues to extend forward along the edge of the secondary phase particles or through the secondary phase particles.

### References

- 1 Yuan Hua, Shen Jian. *Modular Machine Tool & Automatic Manufacturing Technique*[J], 2016(3): 1 (in Chinese)
- 2 Peng Wei, Xiao Tiezhong, Huang Juan. *Machine Tool & Hydraulics*[J], 2018, 46(18): 135
- 3 Xiao Tiezhong, Huang Juan, Luo Jing. *Manufacturing Technology & Machine Tool*[J], 2016(8): 57 (in Chinese)
- 4 Zhang Jinhui, Li Keqiang, Xu Biao et al. *Automotive Engineering*[J], 2018, 40(10): 1151 (in Chinese)
- 5 You Xiaoyue, Lei Xinghui, Shi Yongjiang. *Science and Technology Management Research*[J], 2018(16): 45 (in Chinese)
- 6 Fu Penghuai, Peng Liming, Ding Wenjiang. *Strategic Study of CAE*[J], 2018, 20(16): 84 (in Chinese)
- 7 Sun Wei, Jing Yu, Tong Weiping et al. *Rare Metal Materials and Engineering*[J], 2021, 50(6): 2118 (in Chinese)
- 8 Wei Chao, Liu Guanglei, Wan Hao et al. *High Temperature Materials and Processes*[J], 2018, 37(4), 289
- 9 Ding Wanwu, Xu Chen, Hou Xingang et al. *Journal of Alloys and Compounds*[J], 2019, 776: 904
- 10 Zhang Jie, Zhang Dongqi, Wu Pengwei et al. *Rare Metal Materials and Engineering*[J], 2014, 43(1): 47
- 11 Abedi K, Emamy M. *Materials Science and Engineering A*[J], 2010, 527(16-17): 3733
- 12 Qiu Ke, Wang Richu, Peng Chaoqun et al. *Transactions of Nonferrous Metals Society of China*[J], 2015, 25(11): 3886
- 13 Ghoncheh M H, Shabestar S G, Asgari A et al. *Transactions of Nonferrous Metals Society of China*[J], 2018, 28(5): 848
- 14 Li Ming, Li Yuandong, Bi Guangli. *Transactions of Nonferrous Metals Society of China*[J], 2018, 28(3): 393
- 15 Huang Huilan, Dong Yanheng, Xing Yuan et al. *Journal of Alloys and Compounds*[J], 2018, 765: 1253
- 16 Zhang Jiahong, Xing Shuming, Han Qingyou et al. *Rare Metal Materials and Engineering*[J], 2018, 47(11): 3301
- 17 Lua L, Dahle A K. *Materials Science and Engineering A*[J], 2006, 435-436: 288
- 18 Xiang Xuemei, Lai Yuxiang, Liu Chunhui et al. *Acta Metallurgica Sinica*[J], 2018, 54(9): 1273 (in Chinese)
- 19 Prasada R A K, Das K, Murty B S et al. *Journal of Alloys and Compounds*[J], 2009, 480: L49
- 20 Zhao Hongliang, Song Yong, Li Miao. *Journal of Alloys and Compounds*[J], 2010, 508: 206
- 21 Song Jiajia, Guo Deyan, Deng Chao et al. *Rare Metal Materials and Engineering*[J], 2013, 42(4): 756 (in Chinese)
- 22 Yan Qingsong, Pan Fei, Lu Gang et al. *Rare Metal Materials and Engineering*[J], 2018, 47(6): 1842 (in Chinese)
- 23 Wang Zhengjun, Si Naichao, Wang Hongjian et al. *Rare Metal Materials and Engineering*[J], 2017, 46(1): 164 (in Chinese)
- 24 Guo Bingshan, Zhan Zhangsong, Peng Bo et al. *Transactions of CSICE*[J], 2017, 35(2): 164 (in Chinese)
- 25 Liu Guanglei, Si Naichao, Sun Shaochun et al. *Acta Metallurgica Sinica*[J], 2013, 49(3): 303 (in Chinese)
- 26 Liu Ting, Si Naichao, Liu Guanglei et al. *Transactions of Nonferrous Metals Society of China*[J], 2016, 26(7): 1775
- 27 HB6660-1992[S], 1992 (in Chinese)
- 28 Zeng Qingmei, Shu Delin, Guo Xincheng. *Journal of Anhui Institute of Technology*[J], 1988, 7(2): 63 (in Chinese)
- 29 Kwai S C, Peggy J, Wang Q G. *Materials Science and Engineering A*[J], 2003, 341(1-2): 18
- 30 Xia Pengcheng, Yu Jinjiang, Sun Xiaofeng et al. *Rare Metal Materials and Engineering*[J], 2008, 37(1): 50 (in Chinese)
- 31 Chen Shifu, Ma Huiping, Ju Quan et al. *Journal of Iron and Steel Research*[J]. 2011, 23(3): 29 (in Chinese)
- 32 Su Delin. *Mechanical Properties of Engineering Materials*[M]. Beijing: Machinery Industry Press, 2017 (in Chinese)

## 多元 Al-7Si-0.3Mg 合金热疲劳裂纹萌生与扩展行为

王正军<sup>1,2</sup>, 董 陈<sup>1,2</sup>, 王子洋<sup>1</sup>, 张秋阳<sup>1,2</sup>, 刘静静<sup>1,2</sup>, 陈小岗<sup>1,2</sup>

(1. 淮阴工学院, 江苏 淮安 223003)

(2. 江苏省先进制造技术重点实验室, 江苏 淮安 223003)

**摘 要:** 研究了在不同温度下的3种不同处理状态的多元 Al-7Si-0.3Mg 铝合金热疲劳性能, 提出了用积分方法及割线法计算热疲劳裂纹扩展寿命, 并对合金的热疲劳裂纹生长行为进行了分析。结果表明: 温度变化对多元 Al-7Si-0.3Mg 铝合金的热疲劳裂纹扩展速率有直接的影响, 添加了 Cu、Mn、Ti 等元素的多元 Al-7Si-0.3Mg 合金在细化变质处理和直接细化变质处理后的热疲劳性能优于铸态 Al-7Si-0.3Mg 合金。热疲劳裂纹的萌生需经历一定的孕育期, 裂纹萌生于 V 型缺口处, 当交变热应力超过合金的屈服强度  $\sigma_s$  时, 沿着 V 型缺口的应力集中部位或缺陷处会出现不同类型的热疲劳裂纹, 但有且只有 1 条主裂纹。当裂纹尖端扩展路径与第二相颗粒长轴方向形成小于  $45^\circ$  的夹角时, 裂纹扩展将沿着第二相颗粒的边缘继续向前扩展; 当裂纹尖端扩展路径与第二相颗粒短轴方向形成小于  $45^\circ$  的夹角时, 裂纹将穿过第二相颗粒, 继续向前扩展。

**关键词:** 多元 Al-7Si-0.3Mg 铝合金; 热疲劳; 萌生; 裂纹扩展寿命计算; 扩展路径

作者简介: 王正军, 男, 1975 年生, 博士, 副教授, 淮阴工学院机械与材料工程学院, 江苏 淮安 223003, 电话: 0517-83559196, E-mail: wangzjhyit@hyit.edu.cn